Classical and quantum structures in the kicked-top model

G. M. D'Ariano
Dipartimento di Fisica "Alessandro Volta," Università degli Studi di Pavia via A. Bassi 6, I-27100 Pavia, Italy

L. R. Evangelista*
Dipartimento di Fisica, Politecnico di Torino, Corso Duca degli Abruzzi 24, 10129 Torino, Italy

M. Saraceno†
Service de Physique Théorique, Commissariat à l'Energie Atomique–Centre d'Etudes Nucléaires de Saclay, F-91191 Gif-sur-Yvette CEDEX, France
and Division de Physique Théorique, Institut de Physique Nucléaire, 91406 Orsay CEDEX, France
(Received 1 August 1991)

We study the relationship between classical and quantum structures for a map on the sphere whose behavior can be chaotic in the classical limit. On the classical side we implement an efficient method to locate periodic points on symmetry lines. On the quantum side we show how matrix elements of the propagator in the coherent-state representation are connected to classical structures. Diagonal and off-diagonal matrix elements are related to periodic points, symmetry lines, and other invariant structures in phase space, both in the time and in the energy domains. The scarring phenomena related to the short periodic orbits and their homoclinic neighborhoods are discussed.

PACS number(s): 05.45.+b, 03.40.Kf, 03.65.−w

I. INTRODUCTION

The subtle complexity of the semiclassical limit of quantum-mechanical systems whose classical behavior is chaotic has still to be assessed in its full magnitude. Although the problem was recognized very early in the development of quantum mechanics [1], the basic difficulty remains essentially unsolved: for chaotic systems there is no description of eigenfunctions nor a way to calculate eigenvalues in terms of classical structures that survives the semiclassical limit.

At this stage of our understanding it is then extremely useful to study simple models where these questions can be faced with a minimum of complication and develop methods where the classical and quantum structures appear in a unified setting. Essential characteristics of these models, providing a minimal arena for chaotic motion, are a compact phase space (for mixing) and unstable motions in large regions (for hyperbolicity). Area preservation is the signature of nondissipative dynamics.

The purpose of this paper is to explore the correspondence between the classical structures of a simple map on the sphere and their quantum counterparts. The model [2–4], describing the dynamics of a large spin subject to a magnetic field and an impulsive quadrupole interaction, has been extensively studied: in particular, the time evolution of observables [2], the statistics of the quasienergy-levels [3], and more recently some aspects of the structure of the wave functions [5] have been analyzed.

Using the coherent-state representation we show how periodic points, symmetry lines, and homoclinic and heteroclinic structures arise in the quantum context. A similar study was done recently for the baker's transformation on the torus [6] and our results here complement and extend that work. In spite of having a relatively complicated classical dynamics, the present model is closer to realistic systems than the baker's transformation in that it has a dynamics of mixed type becoming strongly chaotic as a parameter is increased. The advantage is that it is possible to explore the classical-quantum correspondence in a model with nonuniform hyperbolicity and with no discontinuities in the map. The price to pay is, however, a much more complicated classical dynamics. Our principal result is to show how various matrix elements of the propagator in the coherent-state representation reflect the classical structures and how this correspondence is affected by chaotic motion. The methods that we use can be easily adapted to the study of other maps that act on a compact phase space with simple topology and that have time-reversal and parity symmetries.

The paper is organized as follows. In Sec. II we present the model with its symmetries and illustrate an efficient method to numerically locate periodic points on the symmetry lines. We also briefly review the representation of the model in terms of coherent states.

In Sec. III we analyze the correspondence between classical and quantum structures, studying the time evolution of quantum packets and evaluating the matrix elements of the n-step propagator which provide the quantum analogs of either periodic points or symmetry lines. We also study the stationary properties of the quantum propagator in the energy domain, illustrating the relevant scarring mechanisms. Section IV closes the paper with some concluding remarks.

II. QUANTUM AND CLASSICAL MODEL

A. The model

The quantum model [2, 3] describes an angular-momentum vector $\hbar\vec{J} = \hbar(\hat{J}_x, \hat{J}_y, \hat{J}_z)$, $[\hat{J}_i, \hat{J}_j] = i\epsilon_{ijk}\hat{J}_k$

whose dynamics is governed by the Hamiltonian

$$\hat{H}(t) = (\hbar p/T)\hat{J}_z + (\hbar k/2J)\hat{J}_x^2 \sum_{n=-\infty}^{+\infty} \delta(t - nT) . \quad (1)$$

In the Heisenberg picture the time evolution after the discrete times nT (n integer) is obtained by iterating the equation

$$\vec{J}' = \hat{U}\vec{J}\hat{U}^\dagger , \quad (2)$$

where $\hat{U} \equiv \hat{U}(k,p)$ is the Floquet operator

$$\hat{U}(k,p) = \exp[-i(k/2J)\hat{J}_x^2]\exp(-ip\hat{J}_z) . \quad (3)$$

One obtains the quantum iterated map

$$\begin{aligned} \hat{J}_x' &= \hat{J}_x \cos p - \hat{J}_y \sin p , \\ \hat{J}_y' &= \frac{1}{2}(\hat{J}_x \cos p - \hat{J}_y \sin p + i\hat{J}_z)e^{ik(\hat{J}_x'+\frac{1}{2})/J} + \text{H.c.} , \\ \hat{J}_z' &= \frac{1}{2i}(\hat{J}_y \cos p + \hat{J}_x \sin p + i\hat{J}_z)e^{ik(\hat{J}_x'+\frac{1}{2})/J} + \text{H.c.} , \end{aligned} \quad (4)$$

which represents a precession of the angular momentum around the z axis followed by a twist around the x axis. In this fashion the model can be considered as a mapping of the angular-momentum sphere upon itself.

For the remainder of this paper we specialize the map to the case $p = \pi/2$ [2]:

$$\begin{aligned} \hat{J}_x' &= -\hat{J}_y , \\ \hat{J}_y' &= \frac{1}{2}(-\hat{J}_y + i\hat{J}_z)e^{-ik(\hat{J}_y-\frac{1}{2})/J} + \text{H.c.}, \\ \hat{J}_z' &= \frac{1}{2}(\hat{J}_x + i\hat{J}_z)e^{-ik(\hat{J}_y-\frac{1}{2})/J} + \text{H.c.} \end{aligned} \quad (5)$$

The classical Poincaré map corresponding to the quantum map (5) is obtained introducing the rescaled vector $\vec{\omega} = (X,Y,Z) \equiv \vec{J}/J$ and performing the limit $J \to \infty$. One obtains

$$\begin{aligned} X' &= -Y , \\ Y' &= X \cos kY + Z \sin kY , \\ Z' &= Z \cos kY - X \sin kY , \end{aligned} \quad (6)$$

and X, Y, Z are now c-number variables lying on the unit sphere $\vec{\omega}^2 = 1$ (in the following we will denote the point on the unit sphere by ω, dropping the vector notation). The angular-momentum sphere has a natural symplectic structure defined on it, inherited from the orbit structure of the SU(2) group [7]. Here we simply notice that the map (6) is area preserving, the area element being the usual one on the sphere $dS = \sin\theta\, d\theta\, d\phi$. In terms of the canonical coordinates on the sphere (I, ϕ)

$$\begin{aligned} I &\equiv Z = \cos\theta , \\ \phi &= \arctan Y/X , \end{aligned} \quad (7)$$

the Jacobian of the map (6) is

$$\frac{\partial(I',\phi')}{\partial(I,\phi)} = 1 . \quad (8)$$

In the following we will synthetically rewrite the map (6) using the symbolic notation

$$\omega' = M \circ \omega , \quad (9)$$

or, alternately, using the matrix form

$$\omega' = \mathbf{M}(\omega)\omega . \quad (10)$$

The nonlinearity of the action of M is reflected on the fact that the matrix $\mathbf{M}$ depends on ω. One has

$$\mathbf{M}(\omega) = \begin{pmatrix} 0 & -1 & 0 \\ \cos kY & 0 & \sin kY \\ -\sin kY & 0 & \cos kY \end{pmatrix} . \quad (11)$$

B. Symmetries

The discrete symmetries of this map have been discussed by Haake, Kuś, and Scharf [2] in order to locate periodic points. Here we generalize their discussion, implementing an efficient method that allows for a one-dimensional search of periodic points along the iterates of symmetry lines. The method is similar to the one used in connection with the standard map by Ichikawa *et al.* [8–10].

We consider maps that possess two kinds of invariance: a symmetry S of the *"parity"* type, satisfying the equation

$$[M,S] \equiv M \circ S - S \circ M = 0 , \quad (12)$$

and a symmetry T of the *"time-reversal"* type, with the property

$$T \circ M - M^{-1} \circ T = 0 , \quad (13)$$

M^{-1} denoting the map inverse of M, namely $M^{-1} \circ M = M \circ M^{-1} = 1$.

In the case of an iterated map $M_n = M^n = M \circ M \circ \cdots \circ M$ (n times, $n \in Z$), infinite sequences of symmetries $\{S_n\}$ and time-reversal symmetries $\{T_n\}$ [all satisfying Eqs. (12) and (13), respectively] can be generated as follows:

$$S_n = M^n S , \quad (14)$$

$$T_n = M^n T . \quad (15)$$

The iterated symmetries S_n commute

$$[S_n, S_m] = [S_n, S_m^{-1}] = 0 . \quad (16)$$

Every power M^n of the map can be decomposed (in infinitely many ways) into the product of two symmetries or two time-reversal symmetries

$$M^p = S_{n+p}S_n^{-1} , \quad (17)$$

$$M^p = T_{n+p}T_n^{-1} = T_{n+p}^{-1}T_n . \quad (18)$$

The product of two time-reversal operations (in general, not belonging to the same family) is a parity, whereas the product of a parity with a time reversal is a time reversal: in this way new parities or time-reversal operations can be generated, as, for example,

$$\tilde{T} = ST \,, \tag{19}$$

and for $\tilde{T} \notin \{T_n\}$ a new infinite family of time-reversal symmetries $\{\tilde{T}_n\}$ can be obtained using the defining relation (15).

The above analysis has been carried out in the classical context but it is clear that it can be simply generalized to the quantum domain. Here the symmetries are represented by unitary operators (antiunitary for the time-reversal ones) acting on the $2J+1$ representation space, whereas Eqs. (12)–(19) are rewritten by substituting M with the Floquet operator $\hat{U}$ of Eq. (3), the product map becoming now the operator product.

Specifically our model has two independent time-reversal symmetries, which are also involutions ($T^2 = \tilde{T}^2 = 1$), and have the following matrix form:

$$T = \begin{pmatrix} 0 & -1 & 0 \\ -1 & 0 & 0 \\ 0 & 0 & 1 \end{pmatrix} \,, \quad \tilde{T} = \begin{pmatrix} 0 & 1 & 0 \\ 1 & 0 & 0 \\ 0 & 0 & 1 \end{pmatrix} \,. \tag{20}$$

The matrices (20) represent the time-reversal symmetries at the classical level of Eq. (10). They are related to each other through Eq. (19) by the parity

$$S = \begin{pmatrix} -1 & 0 & 0 \\ 0 & -1 & 0 \\ 0 & 0 & 1 \end{pmatrix} \tag{21}$$

representing a π rotation around the z axis. As a consequence of the symmetry S the phase space is divided into two equivalent parts which exhibit the same dynamical evolution (both in the classical and in the quantum cases). Therefore, in the following we will divide the phase space into the two hemispheres $0 \le \phi < \pi$ and $\pi \le \phi < 2\pi$ and represent all the dynamics of the model on the first hemisphere only.

The operators representing the symmetries T, $\tilde{T}$, and S are

$$\hat{T} = \hat{K}\hat{R} \,, \tag{22}$$

$$\hat{\tilde{T}} = \hat{R}\hat{K} \,, \tag{23}$$

$$\hat{S} = \hat{R}^2 \,, \tag{24}$$

where $\hat{R}$ is the rotation of $\pi/2$ around the z axis

$$\hat{R} = \exp\left(-i\frac{\pi}{2}\hat{J}_z\right) \,, \tag{25}$$

and $\hat{K}$ is the charge conjugation $\hat{K}^2 = 1$

$$\langle\psi|\hat{K}\hat{U}\hat{K}|\psi'\rangle = \langle\psi|\hat{U}|\psi'\rangle^* \tag{26}$$

acting on the angular-momentum operators as follows:

$$\begin{aligned} \hat{K}\hat{J}_x\hat{K} &= \hat{J}_x \,, \\ \hat{K}\hat{J}_y\hat{K} &= -\hat{J}_y \,, \\ \hat{K}\hat{J}_z\hat{K} &= \hat{J}_z \,. \end{aligned} \tag{27}$$

The above correspondence is extended to all the iterated symmetries through operator multiplication. The symmetry $\hat{S}$ allows us to factorize the matrix representation of the operator $\hat{U}$ into two blocks, thus reducing the size of the matrix by a factor of 2 in the diagonalization procedure. Notice that the quantum version of the time-reversal symmetries is described by antiunitary operators, and, as a consequence, any matrix realization of the complete symmetry group should be thought of as a group corepresentation [11]. This framework is fully exploited in Ref. [12] for a slightly different kicked-top model, accounting for level-repulsion mechanisms in terms of unitary and antiunitary symmetries.

In concluding this section we point out that new symmetries and time-reversal transformation can be found for the iterated maps M^p which are not symmetries for the one-step map M. This is, for example, the case of the π rotation around the y axis S',

$$S' = \begin{pmatrix} -1 & 0 & 0 \\ 0 & 1 & 0 \\ 0 & 0 & -1 \end{pmatrix} , \tag{28}$$

which is a symmetry for M^2, but not for M. One should notice that the new time-reversal symmetries of M^2 obtained from S', namely $T' = S'T$ and $\tilde{T}' = S'\tilde{T}$, are no longer involutions.

C. Periodic points

The period-n orbits of the map that can be found systematically are those lying on the symmetry lines. In this subsection we briefly illustrate the method that we have adopted to locate such cyclic points numerically.

For an iterated map M on a two-dimensional phase space, the sets of fixed points for the symmetries form lines or isolated points, depending on the rank of the fixed-point equation. We denote by $\Phi(P)$ the set of fixed points of the map P, namely

$$\Phi(P) = \{\omega | P \circ \omega = \omega\} \,. \tag{29}$$

With the above notation $\Phi(M^n)$ denotes the set of cyclic points of order $|n|$ for the map M, whereas $\Phi(S_n)$ and $\Phi(T_n)$ represent the sets of fixed points for the symmetries S_n and the time-reversal transformation T_n, respectively. In the case of the map (6) the nonvacuum sets $\Phi(S_n)$ contain isolated points [S_n given by Eqs. (21) and (14)], whereas $\Phi(T_n)$ and $\Phi(\tilde{T}_n)$ are lines on the sphere [$T_n, \tilde{T}_n$ given by Eqs. (20) and (15)].

Using Eqs. (12)–(18) one can simply check the following inclusions between sets:

$$\Phi(T_n) \cap \Phi(T_{n+p}) \subset \Phi(M^p) \cup \Phi(M^p \circ T^2) \,, \tag{30}$$

$$\Phi(S_n) \cap \Phi(S_{n+p}) \subset \Phi(M^p) \cup \Phi(M^{2n+p} \circ S^2) \,. \tag{31}$$

From Eq. (30) one can see that in the case of an involutive time reversal T the intersections between the time-reversal symmetry lines $\Phi(T_n)$ and $\Phi(T_{n+p})$ are cyclic points of order $|p|$. On the contrary, intersecting symmetry lines of different families of time reversal, one no longer obtains cyclic points only,

$$\Phi(T_n) \cap \Phi(\tilde{T}_{n+p}) \subset \Phi(M^p \circ S) \cup \Phi(M^{2n+p} \circ S^2) \,. \tag{32}$$

The sets $\Phi(S_n)$ are invariant under the action of the map M

$$\begin{aligned} M \circ \Phi(S_n) &= \{\omega | \omega = M \circ S_n \circ M^{-1} \circ \omega\} \\ &= \{\omega | \omega = S_n \circ \omega\} \equiv \Phi(S_n) \,, \end{aligned} \tag{33}$$

$M \circ \Phi(P)$ denoting the mapped set of $\Phi(P)$

$$M \circ \Phi(P) \equiv \{\omega | \omega = M \circ \omega', \omega' = P \circ \omega'\}$$
$$= \{\omega | \omega = M \circ P \circ M^{-1} \circ \omega\} . \quad (34)$$

Notice that in general one has

$$M \circ \Phi(P) \neq \Phi(M \circ P) = \{\omega | \omega = M \circ P \circ \omega\} . \quad (35)$$

The symmetry lines $\Phi(T_n)$ are mapped into each other by M

$$M^p \circ \Phi(T_n) = \Phi(T_{n+2p}) , \quad (36)$$

as follows from Eqs. (13), (15), and (34). Equation (36) allows one to obtain all the symmetry lines of the same time-reversal family by mapping only two lines. In our case, the two families of time-reversal lines $\{\Phi(T_n)\}$ and $\{\Phi(\tilde{T}_n)\}$ can be evaluated by mapping four symmetry lines having the following simple parametric equations $(-1 \leq t \leq 1)$:

$$\Phi(T_0) = \begin{cases} X = -Y = \pm\sqrt{(1-t^2)/2} \\ Z = t , \end{cases} \quad (37)$$

$$\Phi(T_1) = \begin{cases} X = t \\ Y = \pm\sqrt{(1-t^2)}\sin(kt/2) \\ Z = \mp\sqrt{(1-t^2)}\cos(kt/2) , \end{cases} \quad (38)$$

$$\Phi(\tilde{T}_0) = \begin{cases} X = Y = \pm\sqrt{(1-t^2)/2} \\ Z = t , \end{cases} \quad (39)$$

$$\Phi(\tilde{T}_1) = \begin{cases} X = 0 \\ Y = t \\ Z = \mp\sqrt{(1-t^2)} . \end{cases} \quad (40)$$

In Fig. 1 the symmetry lines $\Phi(T_n)$ and $\Phi(\tilde{T}_n)$ for $n = -4$ to 4 and $k = 2, 3$ are plotted. Comparing the symmetry lines for the two different values of k, one can see that they become more and more distorted for increasing k. As a consequence, new intersections arise, representing the onset of new cyclic points.

On the basis of the above framework, we have evaluated the cyclic points by means of a numerical one-dimensional search on the symmetry lines, which can now be simply parametrized through Eqs. (36)–(40). Only the curves $\Phi(T_n)$ and $\Phi(\tilde{T}_n)$, with $-p \leq n \leq p$, are needed to locate the cyclic point of order $|p|$. We should make clear, however, that the method by no means exhausts the search of periodic points of a given period, as, in general, there are also periodic points which do not lie on symmetry lines. In fact, just considering maps where a binary coding is complete—for example, the baker's map—one finds many binary sequences which have no definite symmetry. One could proceed to find new symmetries of the iterated maps, as we pointed out in Eq. (28), but clearly the complexity will become equivalent to that of locating directly the periodic points.

The Lyapunov exponents of the cyclic point have been evaluated resorting to the eigenvalues of the matrix

$$\mathbf{L}_p(\omega) = \mathbf{D}(M^{p-1} \circ \omega)\mathbf{D}(M^{p-2} \circ \omega) \cdots \mathbf{D}(\omega), \quad (41)$$

where

$$\mathbf{D}(\omega) = \frac{\partial[M \circ (\omega)]_i}{\partial X_j} = \begin{pmatrix} 0 & -1 & 0 \\ \cos kY & k(-X\sin kY + Z\cos kY) & \sin kY \\ -\sin kY & k(-X\cos kY - Z\sin kY) & \cos kY \end{pmatrix} , \quad (42)$$

$p > 0$ being the order of the cyclic point. In Figs. 4–6 cyclic points evaluated with the above method are represented. In Tables I–V the cyclic points of order $n \leq 6$ and $k = 2, 3, 6$ are reported, giving the canonical coordinates of a representative point for each cycle, along with the Lyapunov exponent λ and the sign σ of the eigenvalue.

D. Representation of the quantum model in the phase space

The surface of the sphere is the phase space for this model: all the classical structures left invariant by the action of the map (periodic points, tori, homoclinic and heteroclinic tangles, etc.) are objects in this space. Likewise the symmetries and, of course, the motion occur on the sphere. Therefore, it is essential to be able to represent quantum operators and states in the phase space. Such a representation is provided by the coherent states of SU(2) [7] or Bloch states [13]. Here we briefly summa-

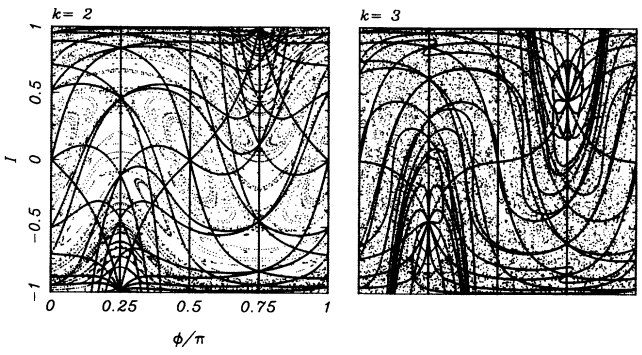

FIG. 1. Classical motion on the phase-space and symmetry lines for $k = 2, 3$. Only the $0 \leq \phi \leq \pi$ hemisphere is represented using the canonical coordinates of Eq. (7). The motion on the other hemisphere $\pi \leq \phi \leq 2\pi$ is an identical replica of the motion on the previous one, due to the symmetry (21). The symmetry lines $\Phi(T_n)$ and $\Phi(\tilde{T}_n)$ are plotted on the classical motion for $n = -4$ to 4.

TABLE I. Cyclic points of order $n \leq 6$ for $k = 2$.

Label	ϕ/π	Z	$n\lambda$	σ
		Order 1		
1	0.000000	−1.000000	0.000000	−
2	0.000000	1.000000	0.000000	+
		Order 3		
1	0.000000	−0.712010	0.664525	+
2	0.365885	−0.331557	*elliptic*	
3	0.365885	−0.331557	*elliptic*	
4	0.250000	−0.117974	0.664524	+
		Order 4		
1	0.500000	0.000000	*elliptic*	
2	0.250000	0.457348	1.870792	+
		Order 5		
1	0.000000	−0.950836	0.126810	+
2	0.162747	−0.774200	0.126809	+
3	0.293001	−0.670048	*elliptic*	
4	0.293002	−0.670048	*elliptic*	
5	0.671014	−0.073387	0.741373	+
6	0.590282	0.199975	*elliptic*	
7	0.590282	0.199975	*elliptic*	
8	0.000000	0.515649	0.741373	+
		Order 6		
1	0.865885	0.331558	*elliptic*	
2	0.500000	0.712011	1.329052	+

rize some of their relevant properties: for a review one can see Ref. [14].

We define the coherent state as

$$|\theta,\phi\rangle_J = e^{2iJ\phi}\left(1+\cot^2\frac{\theta}{2}\right)^{-J} \times \exp\left(e^{-i\phi}\cot\frac{\theta}{2}\hat{J}_+\right)|J,0\rangle. \quad (43)$$

The angles θ and ϕ have the ranges $0 \leq \theta \leq \pi$ and $0 \leq \phi < 2\pi$, respectively. The state $|J,0\rangle$ is the minimum weight state, defined by the property

$$\hat{J}_-|J,0\rangle = 0\ . \quad (44)$$

The representation of the angular-momentum algebra is given by the following equations:

$$\hat{J}_+^n|J,0\rangle = n!\binom{2J}{n}^{1/2}|J,n\rangle\ , \quad (45)$$

$$\hat{J}^2|J,n\rangle = J(J+1)|J,n\rangle\ , \quad (46)$$

$$\hat{J}_z|J,n\rangle = (n-J)|J,n\rangle\ . \quad (47)$$

The index n labels the state of the representation in the range $0 \leq n \leq 2J$.

Using the canonical variables (I,ϕ) and expanding the exponential in Eq. (43), one obtains

$$|I,\phi\rangle_J = \sum_{n=0}^{2J}\sqrt{P_J(I,n)}e^{in\phi}|J,n\rangle\ , \quad (48)$$

where

$$P_J(I,n) = \binom{2J}{n}\left(\frac{1+I}{2}\right)^{2J-n}\left(\frac{1-I}{2}\right)^n \quad (49)$$

are the binomial probabilities. In particular, $P_J(1,n) = \delta_{n,0}$ and $P_J(-1,n) = \delta_{2J-n,0}$.

For large J the binomial distribution becomes asymptotically Gaussian: in this case Eq. (48) shows that the coherent state is a wave packet with angular-momentum

TABLE II. Cyclic points of order $n \leq 6$ for $k = 3$.

Label	ϕ/π	Z	$n\lambda$	σ
		Order 1		
1	0.000000	−1.000000	0.962424	−
2	0.750000	0.455719	*elliptic*	
3	0.750000	0.455719	*elliptic*	
4	0.000000	1.000000	0.962424	+
		Order 2		
1	0.250000	−0.455719	*elliptic*	
		Order 3		
1	0.000000	−0.741739	2.002056	+
2	0.380624	−0.065785	0.991094	−
3	0.380624	−0.065783	0.991092	−
4	0.250000	0.316787	2.002056	+
		Order 4		
1	0.500000	0.000000	*elliptic*	
2	0.249999	0.615950	3.359144	+
		Order 5		
1	1.000000	−0.961906	2.763133	+
2	0.117996	−0.656129	2.763131	+
3	0.682958	−0.423488	3.234221	+
4	0.325946	−0.162380	2.305126	−
5	0.325946	−0.162373	2.305126	−
6	0.589264	0.036256	2.854635	−
7	0.589265	0.036258	2.854634	−
8	0.699379	0.233769	1.473418	+
9	0.699379	0.233770	1.473418	+
10	0.000000	0.649534	3.234223	+
11	0.801832	0.870827	*elliptic*	
12	0.801832	0.870827	*elliptic*	
		Order 6		
1	0.308494	−0.946753	2.706071	+
2	0.154283	−0.917607	2.637740	−
3	0.353056	−0.613621	2.637753	−
4	0.189593	−0.203697	2.706069	+
5	0.856273	−0.187665	0.501092	−
6	0.880624	0.065785	1.982189	+
7	0.143728	0.187665	0.501092	−
8	0.143728	0.187665	0.501092	−
9	0.810407	0.203694	2.706099	+
10	0.899153	0.367352	0.501092	−
11	0.499994	0.741743	4.004123	+
12	0.845718	0.917605	2.637717	−
13	0.845717	0.917606	2.637728	−
14	0.691506	0.946753	2.706070	+

projection distributed around the mean value $\overline{n} = J(I+1)$. It follows that the continuous variable I is the classical analog of the discrete quantum number $(n/J) - 1$ in the limit when $J \to \infty$.

The SU(2) coherent states are the closest analog to phase-space points that can be constructed in the quantum mechanics on the sphere. They are the equivalents of Gaussian wave packets in ordinary phase space. We therefore expect that classical objects will be more easily recognized in this representation.

The coherent states can be used to display the phase-space properties of operators by means of the correspondence

$$\mathcal{A}(I,\phi) = {}_J\langle I,\phi|\hat{A}|I,\phi\rangle_J \ , \tag{50}$$

which is called the Q representation in the literature [14]. When applied to pure-state density operators this definition yields the Husimi distribution of a state $|\psi\rangle_J$,

$$\mathcal{H}_\psi(I,\phi) = |{}_J\langle I,\phi|\psi\rangle_J|^2 \ . \tag{51}$$

It is important at this point to stress that the coherent states provide a full representation of all quantum-mechanical aspects of a given problem, alternative to the position or momentum representation. Moreover, as we will show in the following, they also display the correspondence to classical motion in a most pregnant way.

As a detail of practical interest in numerical computations, we mention that the summation in Eq. (48), and in general all transformations to the coherent-state representation can be greatly speeded up by using fast-Fourier-transform techniques in the numerical evaluation of the ϕ dependence.

TABLE III. Cyclic points of order $n \leq 4$ for $k = 6$.

Label	ϕ/π	Z	$n\lambda$	σ
		Order 1		
1	0.000000	−1.000000	1.762747	−
2	0.750000	−0.316787	1.171221	−
3	0.750000	−0.316787	1.171221	−
4	0.000000	1.000000	1.762747	+
		Order 2		
1	0.250000	−0.672079	2.652564	−
2	0.750000	−0.672078	2.652560	−
3	0.750000	−0.672078	2.652560	−
4	0.250000	0.316786	2.342440	+
5	0.250001	0.672079	2.652559	−
		Order 3		
1	0.500000	−0.898673	4.904953	+
2	0.000000	−0.898672	4.904950	+
3	0.658418	−0.439255	4.018484	+
4	0.658421	−0.439250	4.018487	+
5	0.395737	0.436339	4.173672	−
6	0.395738	0.436339	4.173669	−
7	0.892368	0.871382	4.747360	−
8	0.892367	0.871385	4.747369	−
		Order 4		
1	0.394471	−0.921332	5.879734	+
2	0.500000	−0.851965	6.363503	+
3	0.386613	−0.745923	5.363348	+
4	0.386611	−0.745920	5.363341	+
5	0.813900	−0.542990	5.072454	−
6	0.813905	−0.542972	5.072466	−
7	0.865393	−0.444529	5.879709	+
8	0.354148	−0.257112	1.844670	+
9	0.354148	−0.257112	1.844670	+
10	0.500000	0.000000	*elliptic*	
11	0.038090	0.329600	3.577975	+
12	0.038091	0.329614	3.578148	+
13	0.134604	0.444511	5.879728	+
14	0.313900	0.542995	5.072450	−
15	0.313917	0.543024	5.072410	−
16	0.249994	0.841789	6.594255	+
17	0.500000	0.851965	6.363498	+
18	0.605532	0.921331	5.879726	+

TABLE IV. Cyclic points of order 5 for $k = 6$.

Label	ϕ/π	Z	$n\lambda$	σ
1	1.000000	−0.910679	7.369180	−
2	0.432997	−0.828976	7.940179	−
3	0.432994	−0.828974	7.940259	−
4	0.784552	−0.707979	7.290845	+
5	0.834725	−0.584268	6.948938	−
6	0.834726	−0.584265	6.948938	−
7	0.677081	−0.513833	6.311345	+
8	0.630695	−0.444429	7.666040	+
9	0.665671	−0.435696	6.723130	−
10	0.665685	−0.435672	6.723135	−
11	0.595919	−0.430815	7.412461	−
12	0.999999	−0.387763	5.502050	+
13	1.000000	−0.387751	5.501984	+
14	0.771601	−0.254929	6.311324	+
15	0.819023	−0.036561	5.447877	−
16	0.819026	−0.036509	5.447864	−
17	0.284748	−0.021173	5.165390	+
18	0.174363	−0.007236	4.991317	+
19	0.174363	−0.007222	4.991303	+
20	0.217201	0.215251	6.568134	−
21	0.217213	0.215345	6.568202	−
22	0.370865	0.263597	5.784517	−
23	0.429536	0.402823	5.042503	−
24	0.429534	0.402823	5.042505	−
25	0.424387	0.410039	5.277918	+
26	0.424386	0.410040	5.277913	+
27	0.370882	0.444310	7.681563	−
28	0.129114	0.444316	7.681595	−
29	0.999999	0.463040	5.784466	−
30	0.156874	0.598519	7.014289	+
31	0.156879	0.598536	7.014260	+
32	0.000000	0.626083	5.165436	+
33	0.202198	0.717812	7.369215	−
34	0.500000	0.748693	5.305103	+
35	0.000001	0.748701	5.305146	+
36	0.547821	0.837816	8.012835	+
37	0.547818	0.837818	8.012758	+
38	0.607127	0.883392	7.290848	+

TABLE V. Cyclic points of order 6 for $k = 6$.

Label	ϕ/π	Z	$n\lambda$	σ
1	0.065231	−0.898477	9.087629	+
2	0.434772	−0.898473	9.087682	+
3	0.262741	−0.714416	7.757861	+
4	0.050390	−0.700244	5.572272	+
5	0.050391	−0.700223	5.571920	+
6	0.052199	−0.613132	5.869082	+
7	0.052199	−0.613126	5.868824	+
8	0.689786	−0.534628	7.757763	+
9	0.810212	−0.534600	7.757801	+
10	0.679813	−0.523068	7.456036	−
11	0.679814	−0.523065	7.456038	−
12	0.895740	−0.436326	8.347362	+
13	0.499999	−0.419761	7.447874	+
14	0.939075	−0.386873	6.870165	+
15	0.059352	−0.330561	6.132602	−
16	0.723371	−0.237868	8.211235	+
17	0.885338	−0.133627	6.132596	−
18	0.677317	−0.012839	6.960819	+
19	0.322684	0.012842	6.960521	+
20	0.114661	0.133610	6.132009	−
21	0.293289	0.172322	6.869868	+
22	0.235697	0.221074	7.455940	−
23	0.276630	0.237872	8.211120	+
24	0.940648	0.330568	6.132355	−
25	0.060925	0.386870	6.869919	+
26	0.499998	0.419765	7.447797	+
27	0.499984	0.419785	7.447941	+
28	0.086970	0.423025	8.678589	+
29	0.158418	0.439242	8.036966	+
30	0.130037	0.444375	9.434880	+
31	0.179809	0.523064	7.456025	−
32	0.310220	0.534638	7.757761	+
33	0.947801	0.613133	5.868972	+
34	0.947801	0.613135	5.869113	+
35	0.949610	0.700257	5.572232	+
36	0.949612	0.700296	5.573028	+
37	0.270748	0.856408	8.822502	−
38	0.565233	0.898472	9.087563	+
39	0.499998	0.898674	9.809863	+
40	0.500000	0.950135	7.447840	+

III. CORRESPONDENCE OF CLASSICAL AND QUANTUM STRUCTURES

A. Evolution of quantum wave packets

The correspondence between classical and quantum evolution can best be studied by means of the action of the map on the coherent states, namely the quantum states that better resemble the classical ones. The resulting evolution of the wave packet—which will not lead in general to a coherent state anymore—can be represented in phase space by its Husimi distribution (51) and then compared to the classical evolution. In Fig. 2 we study the evolution of a coherent state located on the fixed point at the south pole $I_0 = -1$. For $k = 6$ this fixed point is unstable and has a Lyapunov exponent $\lambda = 1.763$. We plot the quantity

$$\mathcal{W}_n(I,\phi) = |{}_J\langle I,\phi|\hat{U}^n|I_0,\phi_0\rangle_J|^2 \tag{52}$$

for successive times $n = 1,\ldots,6$ and as a function of (I,ϕ). Initially the quantum behavior is indistinguishable from the classical evolution of a small cluster of points. The distribution expands exponentially along the unstable manifold W^+ while shrinking in the direction of the stable one W^-. The rate of expansion is governed by the Lyapunov exponent λ. The repeated folding of the unstable manifold, characteristic of the motion in a hyperbolic region is clearly visible. At later times interference effects take over and the resulting classical and quantum distributions become completely different.

The time n^* at which this transition occurs has been estimated with an argument which relates the stretching to the finiteness of the available phase space [15]. It yields

$$n^* \simeq \frac{\ln(2J+1)}{\lambda} \simeq 4\,. \tag{53}$$

The fact that a sharp transition in the structure of the propagator is occurring at time n^* can be more clearly seen in a different representation, recently proposed by Leboeuf and Voros [16]. The representation makes use

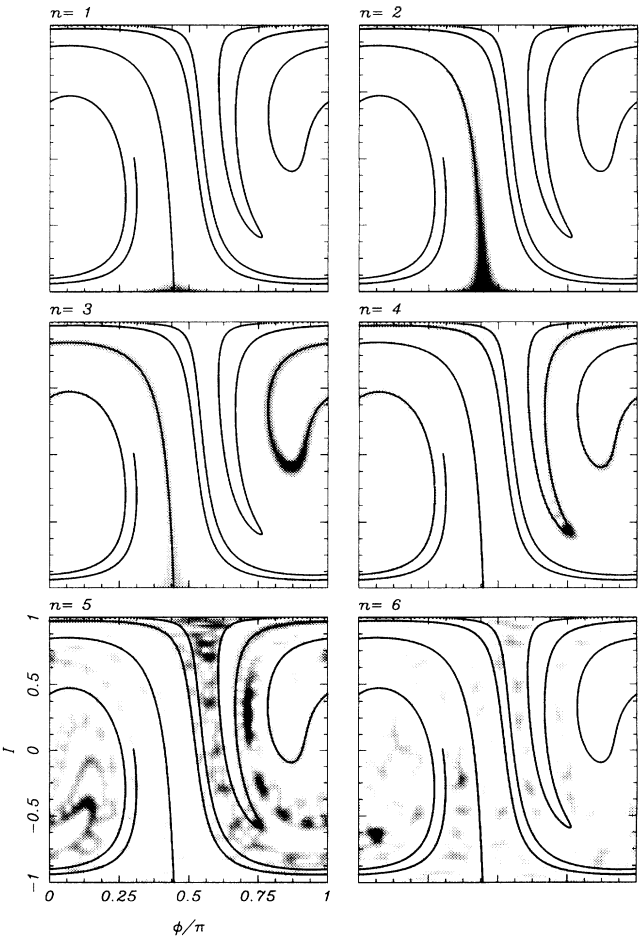

FIG. 2. Evolution of the coherent wave packet $|J,0\rangle$ centered at the southern pole for $k = 6$ and $2J + 1 = 1024$. The line is the unstable manifold and the shades of gray are proportional to the value of $\mathcal{W}_n$ in Eq. (52).

of the fact that the coherent state (43) is analytic in the variable $z = e^{i\phi}\cot(\theta/2)$ (when normalization is disregarded). In fact, it is just a polynomial of degree $2J$, which can be factorized over its zeros. Thus any pure quantum-mechanical state can be fully characterized by $2J$ points in phase space whose motion fully determines the quantum evolution [17]. In our case the quantity $|_J\langle I,\phi|\hat{U}^n|I_0,\phi_0\rangle_J|^2$ for fixed initial variables is analytic in the final ones and its zeros can be used as an alternative to the Husimi distribution for the phase-space display of the propagator.

In Fig. 3 we show the transition region around $n^* \simeq 5$ for the same situation as in Fig. 2, but now showing the position of the zeros. The drastic change in organization is clearly seen at $n^* \simeq 5$. The zeros are neatly lined up in between the folds of the unstable manifold at $n = 3$ and 4. At $n = 6$ the distribution does not seem to have any discernible pattern.

B. Periodic points

Periodic points are the simpler invariant structures left in the classical motion when tori have been destroyed. Therefore, they provide the strongest candidates for a link between classical and quantum invariant structures in the chaotic regime. In fact, the only known representation of the density of states in terms of classical objects is the Gutzwiller's periodic-orbit sum [18, 19], which, however, has serious convergence and interpretation problems in the chaotic regime [20].

Periodic points appear in quantum mechanics when we compute the coherent-state mean value of the n-step propagator

$$\mathcal{P}_n(I,\phi) = {}_J\langle I,\phi|\hat{U}^n|I,\phi\rangle_J \ . \tag{54}$$

The argument for this is quite simple and relies on a semiclassical image of the propagation: the center of the wave packet will approximately follow a classical trajectory and therefore $\mathcal{P}_n$ will be large when $|I,\phi\rangle_J$ is centered on an n-periodic point.

Heller [21] has studied extensively the autocorrelation (54) as a function of time, and derived important results on the scarring of the eigenfunctions originating from a specific periodic orbit. Here we study it for a fixed n and as a function of the point in the phase-space. Heller's analysis gives an approximate value for the autocorrelation function at hyperbolic periodic points

$$|\mathcal{P}_n(I,\phi)|^2 \simeq \frac{1}{\cosh \lambda n} \tag{55}$$

in terms of the Lyapunov exponent λ. Therefore, we expect the phase-space plot of $|\mathcal{P}_n|^2$ to show peaks at the isolated periodic points of period n with heights decreasing very rapidly with λn.

This expectation is strikingly brought out in Fig. 4, where we show the plots of $|\mathcal{P}_n|^2$ for $n = 1, \ldots, 6$, $k = 3$,

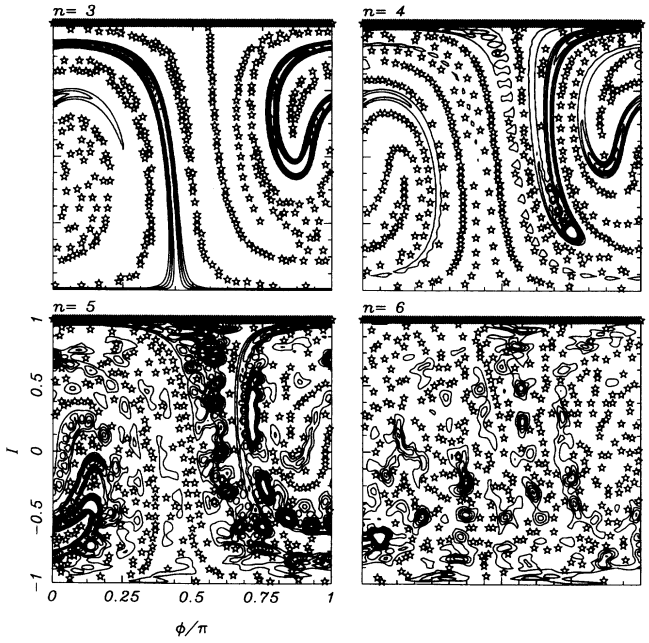

FIG. 3. Evolution of the wave packet (as in Fig. 2) near the transition region $n \simeq n^*$. The contours of $\mathcal{W}_n$ in Eq. (52) are drawn: the small stars give the position of the zeros.

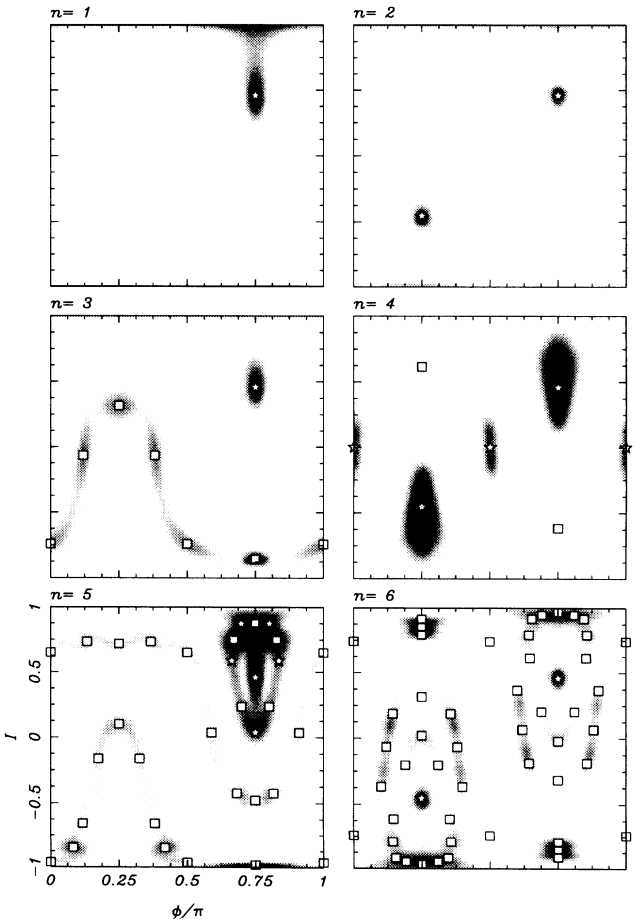

FIG. 4. Quantum autocorrelation function $|\mathcal{P}_n|^2$ in Eq. (54) and corresponding cyclic points for $n = 1$–6, $k = 3$, and $2J + 1 = 256$. The boxes give the hyperbolic periodic points while the stars give the elliptic ones.

and $2J+1=256$. In the figures we have also plotted the periodic points from Table II. A great deal of classical information can be revealed by a detailed analysis of Fig. 4. The first thing we notice is that the even powers have the extra symmetry that exchanges the north and south poles [S' of Eq. (28)], whereas the odd powers do not. The elliptic point first appearing for $n=1$ at $I=0.456$, $\phi=3\pi/4$ reappears at all powers of the map and generates around it an island structure of alternating elliptic and hyperbolic points characteristic of broken Kolmogorov-Arnold-Moser (KAM) tori. This is clearly shown at $n=5$. Already at $n=6$ the stable points have disappeared and have been replaced by all hyperbolic points (some with reflection), whose organization resembles that of the destroyed tori, being now in a strongly chaotic region.

The elliptic point that first appears for $n=2$ at $I=-0.456$, $\phi=\pi/4$ (whose companion is at $I=-0.456$, $\phi=5\pi/4$) is only seen for even powers of the map, but generates structures visible for $n=3,4,5$. The chain of hyperbolic points clearly seen at $n=3$ is likewise a remnant of a chain of islands around this elliptic point. At period 4 there appears the only point (on the equator $I=0$) that remains elliptic regardless of the value of the parameter k. The relative intensities of the peaks also correspond approximately with Eq. (55).

When longer times are considered, the different peaks corresponding to each periodic point start to coalesce and form other structures that are quite different in the regular and chaotic regions. In Fig. 5 we show the $n=11$ iteration for $k=2$ and $2J+1=128$, corresponding to a nearly integrable case. The classical periodic points lie in very close correspondence to the broken rational tori and show the characteristic alternation of elliptic and hyperbolic points. The quantum distribution does not distinguish anymore the individual periodic points, but shows a collective contribution from the torus with the right frequency. Once this transition has taken place, there are no more surprises in the large-n iterations of the map; only more and more periodic points contribute, but the result is better understood as a torus contribution leading to the known EBK formula [22, 23].

The situation is very different in the chaotic regime. Here the correspondence between periodic points and the propagator is lost after a time n^*, and is replaced by a complex interference pattern arising from the exponentially increasing number of trajectories that explore the neighborhood of a periodic point. No simple representation of these patterns is known and even its adequacy could be doubted in view of the fact that structures extremely small compared to a quantum cell are being invoked. However, some extremely encouraging numerical results have been recently obtained by Tomsovic and Heller for the stadium billiard [24] and by O'Connor, Tomsovic, and Heller for the baker's transformation [25] concerning the long-time accuracy of such a description. An example of this complex behavior is given in Fig. 6, where we show $\mathcal{P}_n$ for a fully chaotic regime at $k=6$. Whereas some quantum peaks can be ascribed to periodic points the main structure is not simply related to the classical one.

C. Symmetry lines

The quantum images of the symmetry lines discussed in Sec. II B can be obtained from the quantities

$$\mathcal{T}_n(I,\phi) = {}_J\langle I,\phi|\hat{T}\hat{U}^n|I,\phi\rangle_J\ , \tag{56}$$

$$\tilde{\mathcal{T}}_n(I,\phi) = {}_J\langle I,\phi|\hat{\tilde{T}}\hat{U}^n|I,\phi\rangle_J\ , \tag{57}$$

where $\hat{\tilde{T}}$ and $\hat{T}$ are given in Eqs. (22) and (23). The argument is analogous to that for periodic points: as long as the propagation is semiclassical, $\mathcal{T}_n$ and $\tilde{\mathcal{T}}_n$ will be large when the wave packet is launched on a symmetry line, because after a time n it will have a large overlap with its time-reversed partner. Thus $\mathcal{T}_n$ and $\tilde{\mathcal{T}}_n$ provide the quantum images of the symmetry lines $\Phi(T_n)$ and $\Phi(\tilde{T}_n)$, respectively. In Fig. 7 we show the precise correspondence between $\mathcal{T}_n$ and $\Phi(T_n)$ for $k=3$ and $2J+1=128$. For long times the correspondence is lost in the same way and for the same reason as in the propagation of wave packets in Sec. III A. The successive foldings in the iterations of the four basic symmetry lines (37)–(40) eventually interfere and the lines are broken up. This process starts at $n=4$ in Fig. 7 and is fully developed in Fig. 8. Notice the similarity with Fig. 3 in the breakup process. The time n^* for this case is $n^*=5$.

The quantities $\mathcal{W}_n,\mathcal{P}_n$ and $\mathcal{T}_n,\tilde{\mathcal{T}}_n$ are all particular

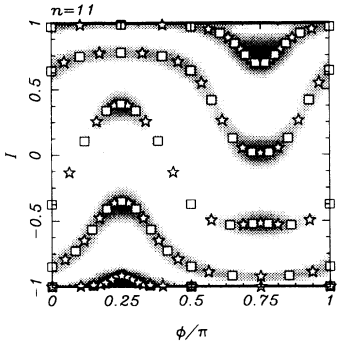

FIG. 5. The same as in Fig. 4 for $n=11$, $k=2$, and $2J+1=128$.

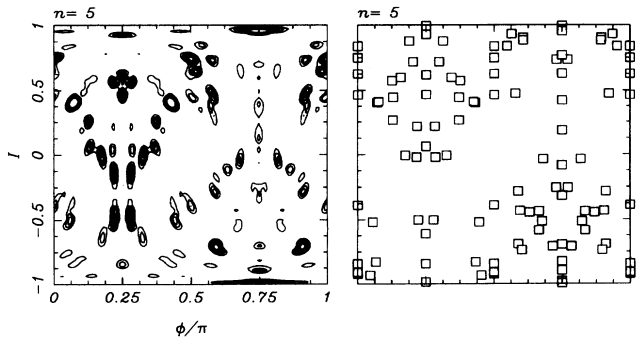

FIG. 6. The same as in Fig. 4 for $n=5$, $k=6$, and $2J+1=1024$.

values of the full quantum time-dependent propagator in the coherent-state representation ${}_J\langle I,\phi|\hat{U}^n|I',\phi'\rangle_J$: these matrix elements, when taken all together, give a very appealing classical interpretation as long as $n \leq n^*$. Thus diagonal elements give the position and stabilities of periodic points, whereas special off-diagonal elements between time-reversed states give images of the symmetry lines. The full complexity of the propagator begins to appear in the off-diagonal elements displaying the unstable manifolds of periodic points (clearly the stable manifold would be displayed if we were to consider $\mathcal{W}_{-n}$). Some theoretical understanding of the full propagator as an object depending on two arbitrary phase-space points has recently been advanced [26] in connection with the kicked-rotor propagation, but a detailed understanding, especially in the chaotic region, is still lacking.

D. Stationary properties of the propagator

In the previous sections we studied several time-dependent properties of the propagator, relating them with classical objects. Now we proceed to study the stationary properties, namely the Fourier transform of the propagator.

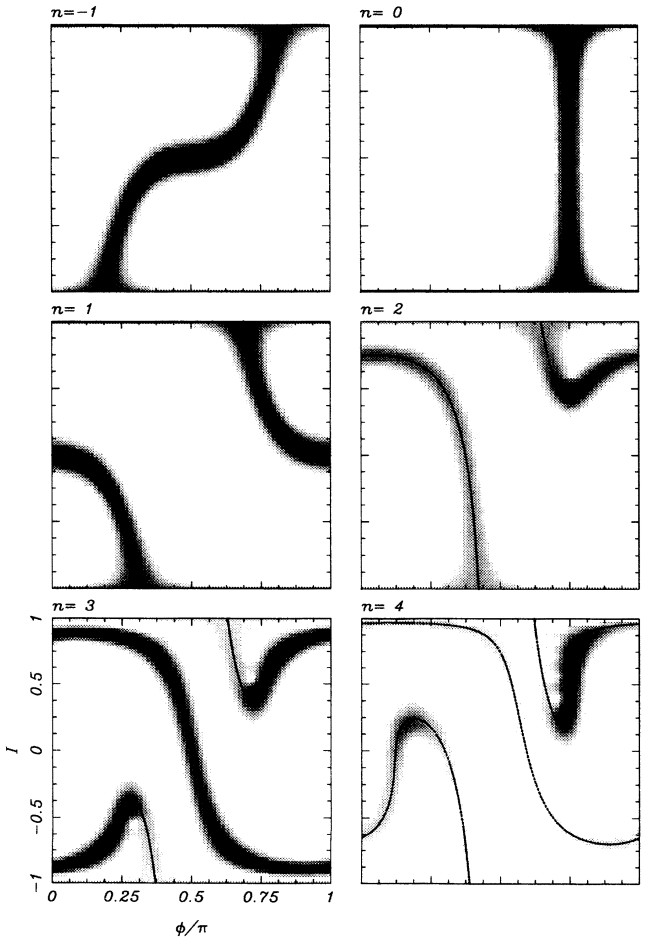

FIG. 7. Quantum symmetry lines $\mathcal{T}_n$ in Eq. (56) and corresponding classical symmetry lines $\Phi(T_{-1})$ [Eqs. (15), (29), (37), and (38)] for $k = 3$, $n = -1$ to 4, and $2J+1 = 128$.

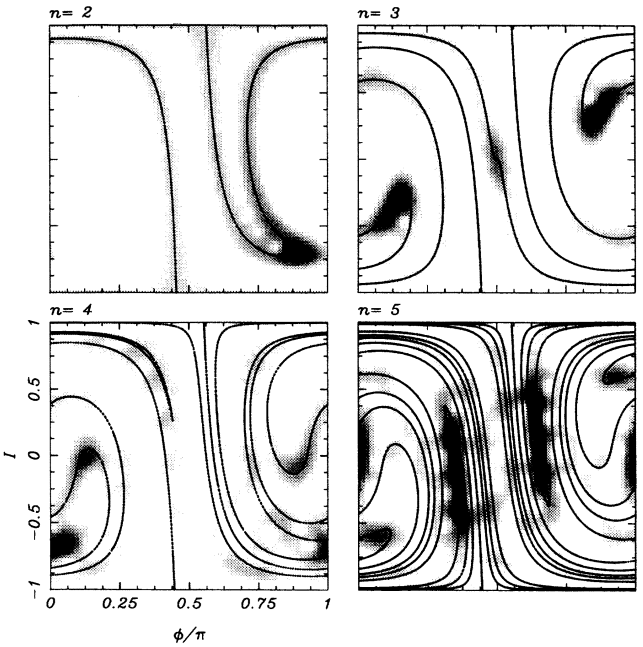

FIG. 8. The same as in Fig. 7 for $k = 6$, $n = 2$–5, and $2J + 1 = 128$.

To avoid the problems related to long-time behavior we use a time cutoff function $f_K(n)$ and define the smoothed spectral intensity operator as

$$\hat{G}_K(\varepsilon) = \sum_{n=-\infty}^{\infty} e^{i\varepsilon n}\hat{U}^n f_K(n) = \sum_{i=0}^{2J} |\psi_i\rangle g_K(\varepsilon - \lambda_i)\langle\psi_i| , \tag{58}$$

where

$$g_K(\varepsilon) = \sum_{n=-\infty}^{\infty} e^{i\varepsilon n} f_K(n) ,$$
$$f_K(n) = \frac{1}{2\pi}\int_0^{2\pi} e^{-i\varepsilon n} g_K(\varepsilon) , \tag{59}$$

and where the spectral decomposition of $\hat{U}$ is used

$$\hat{U}|\psi_i\rangle = e^{-i\lambda_i}|\psi_i\rangle . \tag{60}$$

The precise form of the functions g_K, f_K is not very important as long as they are Fourier transforms of each other. It will be convenient to think of $f_K(n)$ as a Gaussian $f_K(n) = e^{-n^2/2K^2}$ characterized by a time K that provides the desired cutoff. In this case $g_K(\varepsilon)$ is a periodicized Gaussian with width $2\pi/K$. Clearly when $K \to \infty$, $\hat{G}_K(\varepsilon)$ has δ-function singularities at the spectrum.

$\hat{G}_K(\varepsilon)$ can now be studied in the coherent-state representation

$$ {}_J\langle I,\phi|\hat{G}_K(\varepsilon)|I,\phi\rangle_J = \sum_{i=0}^{2J} g_K(\varepsilon-\lambda_i)\mathcal{H}_i(I,\phi) \qquad (61) $$

$$ = \sum_{n=-\infty}^{\infty} e^{i\varepsilon n} f_K(n)\mathcal{P}_n(I,\phi)\,, \qquad (62) $$

where $\mathcal{H}_i(I,\phi)$ is the Husimi distribution (51) of the eigenstates. The above equation provides a link between the quantities $\mathcal{P}_n$ studied in Sec. III B and the smoothed properties of the Husimi distributions of eigenstates. By changing K we can then go continuously from the average properties ruled by the very short times to the properties of a single eigenstate, determined in principle by infinite times.

The following scenario is expected as K is increased. For very small K the sum in (61) involves all the eigenstates and therefore simply by completeness an almost uniform featureless distribution is expected for all values of ε. This is essentially a Weyl term and is trivial as it applies to this map. As K increases the distribution acquires more and more oscillations, corresponding to the peaks in $\mathcal{P}_n(I,\phi)$. As long as the peaks remain isolated the only possibility for interference in the sum (62) is among repetitions of a given trajectory. Heller [21] has provided a very detailed study of the resulting oscillations and decay for a fixed phase-space point on a periodic orbit as a function of ε. The corresponding response function is dominated by two time scales: the period n providing oscillations and the Lyapunov exponent giving a width to the peaks. When the condition $\lambda n \simeq 2\pi$ is fulfilled the oscillations become overdamped and therefore unobservable.

A cursory examination of Tables I–V shows that most of the periodic points listed there should produce visible structures (except the periods 5 and 6 for $k = 6$). We postpone for the time being the analysis of the response functions of periodic points to continue the discussion on the structure of ${}_J\langle I,\phi|\hat{G}_K(\varepsilon)|I,\phi\rangle_J$. As K is increased beyond the time n^* discussed in Sec. III A, interference effects occur not only between a periodic point and its repetitions, but also between nearby periodic trajectories. Thus the phase-space organization and relative phases of the trajectories become crucial for the resulting structure and it is at this point that widely different behavior is to be expected for regular or chaotic regions. In the regular region long periodic trajectories are organized on the invariant tori and produce a collective enhancement near the EBK torus [22, 23]. At this stage of the "unsmoothing" process we then expect to see broad tori in the regular region, which become more sharply defined as the unsmoothing proceeds. In the chaotic region the oscillations related to the short and less unstable periodic orbits become more complicated as these start proliferating exponentially, and the nature of their collective contribution and whether it is related to classical structures is largely unknown.

In Fig. 9 we show ${}_J\langle I.\phi|\hat{G}_K(\varepsilon)|I,\phi\rangle_J$ for $k = 3$ and for some values of ε and the smoothing time K, comparing it to a classical phase-space diagram. In the first frame we show the classical phase-space organization. The most notable structures are the stable islands around the period-1, -2, and -4 elliptic points and a large area of chaotic motion. We have also drawn the manifolds of the unstable fixed points at $I = -1$. The three frames for $K = 12$ show the partially smoothed $\hat{G}_K(\varepsilon)$ at different quasienergies chosen to select structures in different regions. Very visible are the tori in the elliptic islands and the background intensity (not quite featureless) in the chaotic region. The last three frames show the effect of the smoothing at a fixed quasienergy $\varepsilon/2\pi = 0.7189$. At $K = 6$ most of the structures still remaining at $K = 12$ have disappeared leaving only some traces of the elliptic regions. At the opposite extreme for $K = 1000$ a single eigenstate is selected, precisely located on the unstable fixed point and on its stable and unstable manifolds. This is then an example of a strongly "scarred" state, of the same type as observed in the stadium eigenfunctions [27] and in the baker's transformation [6], residing mainly on an unstable trajectory and its hyperbolic neighborhood.

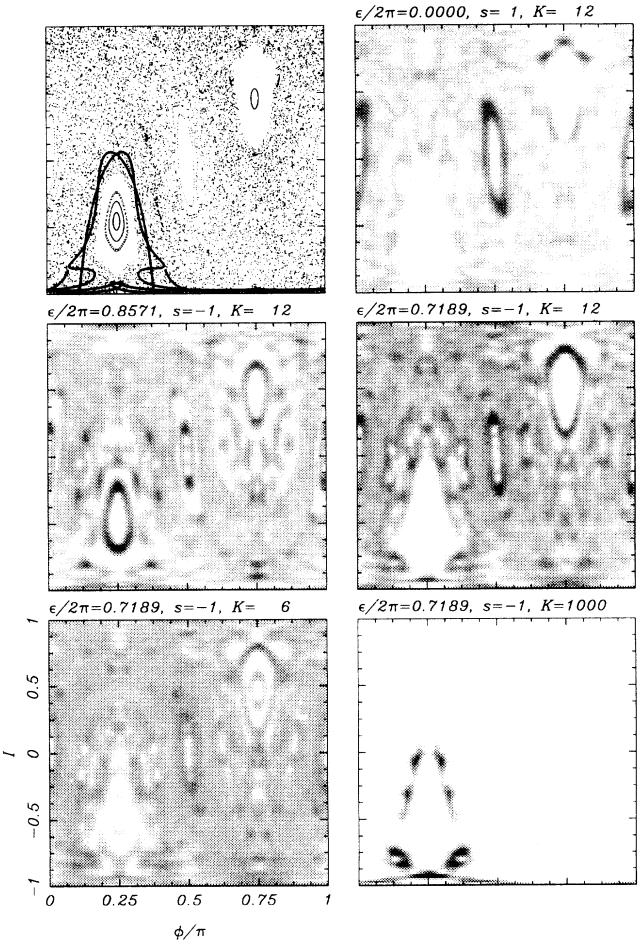

FIG. 9. Smoothed spectral intensity of Eq. (61) for $k = 3$, $2J + 1 = 1024$, and for some values of ε and smoothing time K. Only a parity $s = \pm 1$ corresponding to the eigenvalues of $\exp(-i\pi J)\hat{S}$ in Eq. (24) is selected (the phase factor in the parity definition has been added in order to avoid imaginary eigenvalues for half-odd J.) In the first frame a comparison to the classical phase-space diagram is given, and the stable and unstable manifolds of the $I = -1$ fixed point are drawn.

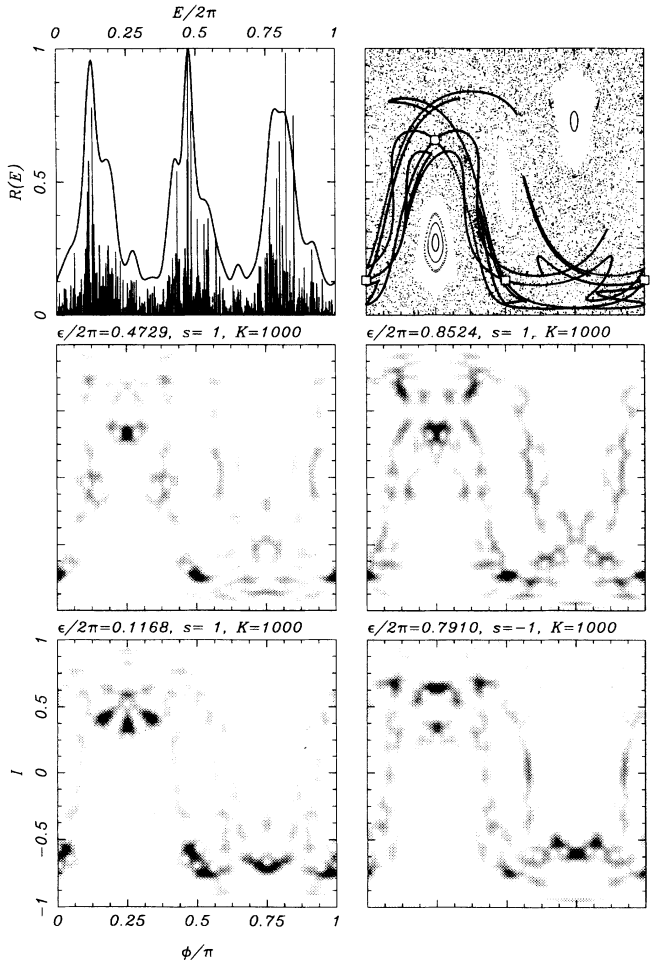

FIG. 10. Response $\hat{G}_K(\varepsilon)$ for the period-3 point at $I = -0.7417$, $\phi = 2\pi$ for $k = 3$, $K = 12$, and $2J + 1 = 1024$; phase-space diagram with the stable and unstable manifolds of the cycle; and phase-space structure of four scarred states with the largest overlap.

In Fig. 10 we analyze the scarring in more detail. We show in the first frame the response $\hat{G}_K(\varepsilon)$ for the period-3 point at $I = -0.7417$, $\phi = 2\pi$, showing that it scars—i.e., it has a large overlap—with three groups of eigenstates. The width ΔE of the structures is related to the Lyapunov exponent [21] by

$$\frac{\Delta E}{2\pi} = \frac{\lambda}{2\pi} = 0.1 \tag{63}$$

and its value coincides very well with $3\lambda = 2.002$ given in Table II. In the second frame we show the homoclinic tangle of the period-3 periodic point and in the rest the four states with the largest overlap. All of them show strong imprints of not only the periodic trajectory but also of its manifolds and their homoclinic intersections. There is at present no way of calculating which state will show a specific scar, except for the broad quasienergy region where it can be expected to be calculated semiclassically [21]. It is quite clear that beside the periodic point the eigenfunctions show also a definite structure around it that traces the homoclinic intersections and recurs at different points with different intensities. In the study of the baker's transformation [6] it was observed that homoclinic points and stable and unstable manifolds were apparent in many of the eigenfunctions. Here we find the manifestation of the same phenomenon occurring in the context of this model in a much more complicated setting.

IV. CONCLUSIONS

We have shown how various matrix elements of the propagator in the coherent-state representation are related to classical properties and how this relationship is consistently lost in the chaotic regime for times n^* of the order $\ln(2J + 1)/\lambda$. Periodic points are displayed by diagonal matrix elements while off-diagonal ones show in general the stable and unstable manifolds. The analyticity of the propagator in each of the initial or final phase-space variables can be exploited to display the zeros of the propagator, in analogy with the recent work of Refs. [16, 17]. Again, it is found that the organization of the zeros changes drastically at the critical time. Symmetry lines and their iterates are obtained in special off-diagonal elements between time-reversed states. In the energy domain the smoothed spectral intensity operator provides the correspondence with invariant structures, but only in an energy-averaged sense. When one tries to uncover the properties of single eigenstates the difficulties inherent in the long-time semiclassical dynamics reappear.

The response function of coherent states on periodic points shows the groups of levels scarred by the periodic point, and the most scarred states show, besides the periodic point, the homoclinic structure that was also observed for the baker's transformation in Ref. [6]. This then appears as a rather general feature in the structure of chaotic eigenfunctions that remains to be explained.

ACKNOWLEDGMENTS

This research was supported by Istituto Nazionale di Fisica Nucleare, CNPq, Brazil, and CEA and CNRS, France. The ICTP, Trieste provided the initial meeting ground and is gratefully acknowledged.

* Permanent address: Departamento de Física, Universidade Estadual de Maringá, 87020 Maringá, Paraná, Brazil.

† Permanent address: Departamento de Fisica, Comisión Nacional de Energia Atomica, 1429 Buenos Aires, Argentina.

[1] A. Einstein, Verh. Dtsch. Phys. Ges. **19**, 82 (1917).
[2] F. Haake, M. Kuś, and R. Scharf, Z. Phys. B **65**, 381 (1987).
[3] H. Frahm and H. J. Mikeska, Z. Phys. B **65**, 249 (1986).
[4] K. Nakamura, Y. Okazaki, and A. R. Bishop, Phys. Rev. Lett. **57**, 5 (1986).

[5] M. Kuś, J. Zakrewski, and K. Życzkowski, Phys. Rev. A **43**, 4244 (1991).
[6] M. Saraceno, Ann. Phys. (N.Y.) **193**, 37 (1990).
[7] A. Cavalli, G. D'Ariano, and L. Michel, Ann. Inst. Poincaré Phys. Theor. **44**, 173 (1986).
[8] Y. H. Ichikawa, T. Kanimura, T. Hatori, and S. Y. Kim, Prog. Theor. Phys. Suppl. **98**, 1 (1989).
[9] E. Piña and L. Jiménez Lara, Physica D **26**, 369 (1987).
[10] G. D. Birkhoff, *Dynamical Systems* (American Mathematical Society, Providence, RI, 1927), p. 186.
[11] E. Wigner, *Group Theory and its Application to the Quantum Mechanics of Atomic Spectra* (Academic, New York, 1959).
[12] M. Kuś, R. Scharf, and F. Haake, Z. Phys. B **66**, 129 (1987).
[13] F. T. Arecchi, E. Courtens, R. Gilmore, and H. Thomas, Phys. Rev. A **6**, 2211 (1985).
[14] A. Perelomov, *Generalized Coherent States* (Springer-Verlag, Berlin, 1986).
[15] M. V. Berry, N.L. Balzas, M. Tabor, and A. Voros, Ann. Phys. (N.Y.) **122**, 26 (1979).
[16] P. Leboeuf and A. Voros, J. Phys. A **23**, 1765 (1990).
[17] P. Leboeuf, preprint Institut de Physique Nucleaire, Report No. IPNO/TH 91-20, 1991 (unpublished).
[18] M. C. Gutzwiller, J. Math. Phys. **12**, 343 (1971).
[19] M. Tabor, Physica **6**, 195 (1983).
[20] A. Voros, J. Phys. A **21**, 685 (1988).
[21] E. J. Heller, in *Chaos and Quantum Physics*, 1989 Les Houches Lectures, edited by A. Voros, M. Giannoni, and O. Bohigas (North-Holland, Amsterdam, 1990).
[22] M. V. Berry and M. Tabor, Proc. R. Soc. London Ser. A **349**, 101 (1976).
[23] A. M. Ozorio de Almeida and J. H. Hannay, J. Phys. A **20** 5873 (1987).
[24] S. Tomsovic and E. J. Heller (unpublished).
[25] P. W. O'Connor, S. Tomsovic, and E. J. Heller (unpublished).
[26] S. Adachi, Ann. Phys. (N.Y.) **195**, 45 (1989); D. Huber, E. J. Heller, and R. Littlejohn, J. Chem. Phys. **89**, 2003 (1988).
[27] E. J. Heller, Phys. Rev. Lett. **53**, 1515 (1984).

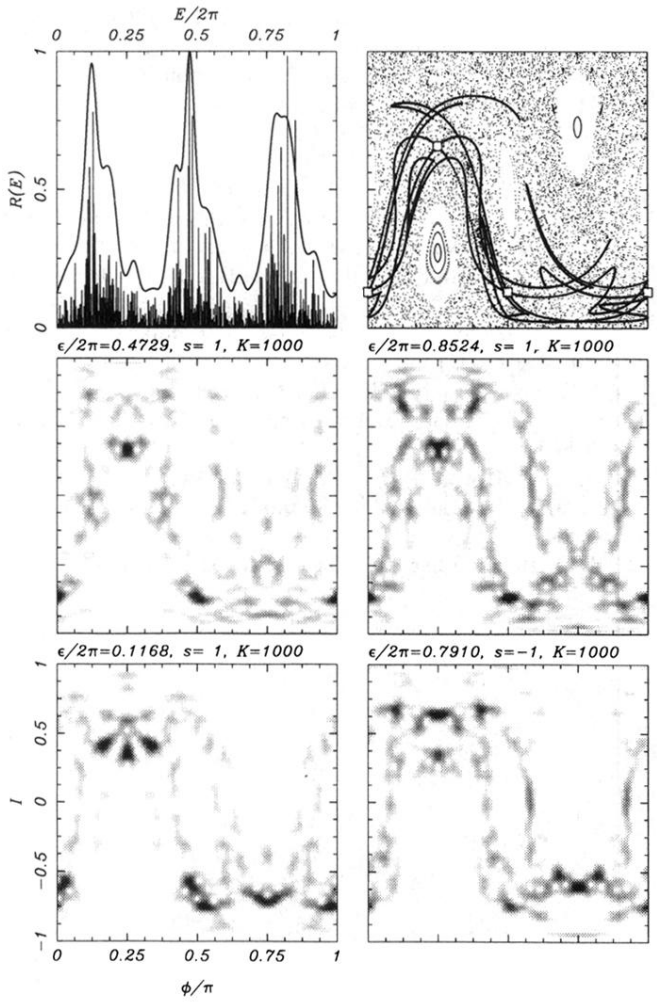

FIG. 10. Response $\hat{G}_K(\epsilon)$ for the period-3 point at $I = -0.7417$, $\phi = 2\pi$ for $k = 3$, $K = 12$, and $2J + 1 = 1024$; phase-space diagram with the stable and unstable manifolds of the cycle; and phase-space structure of four scarred states with the largest overlap.

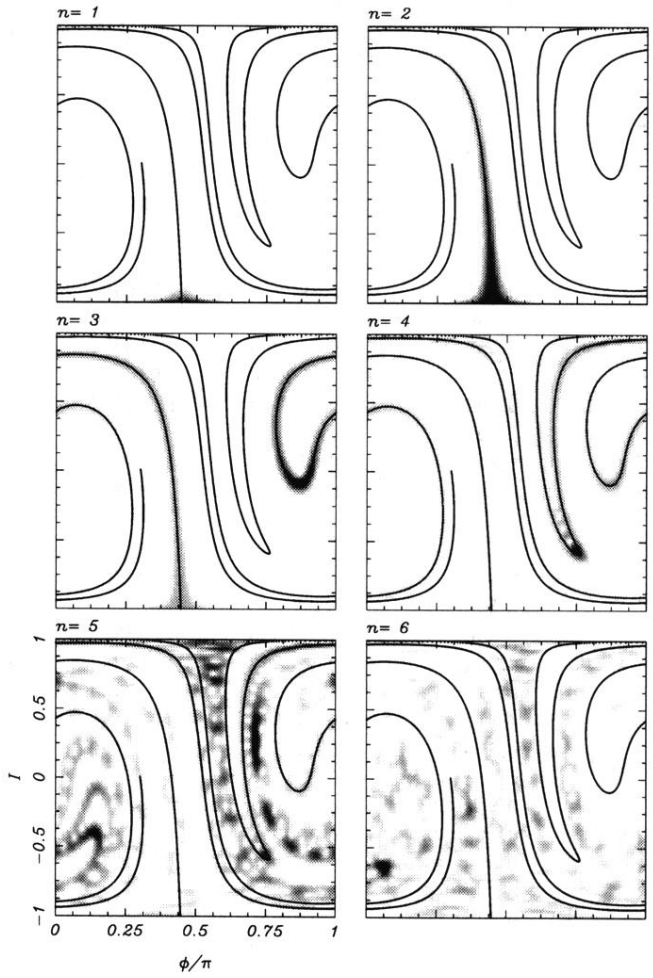

FIG. 2. Evolution of the coherent wave packet $|J, 0\rangle$ centered at the southern pole for $k = 6$ and $2J + 1 = 1024$. The line is the unstable manifold and the shades of gray are proportional to the value of $\mathcal{W}_n$ in Eq. (52).

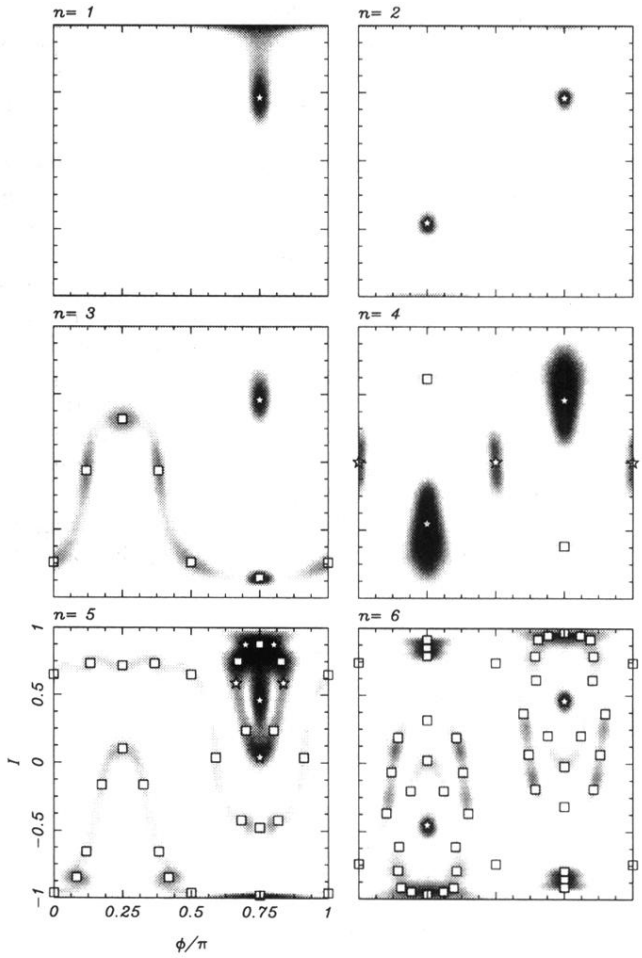

FIG. 4. Quantum autocorrelation function $|\mathcal{P}_n|^2$ in Eq. (54) and corresponding cyclic points for $n = 1$–6, $k = 3$, and $2J + 1 = 256$. The boxes give the hyperbolic periodic points while the stars give the elliptic ones.

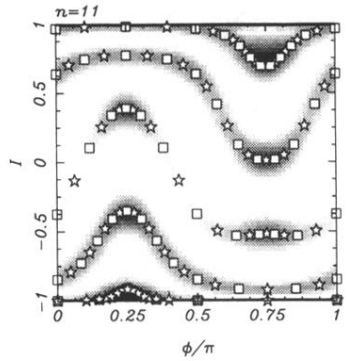

FIG. 5. The same as in Fig. 4 for $n = 11$, $k = 2$, and $2J + 1 = 128$.

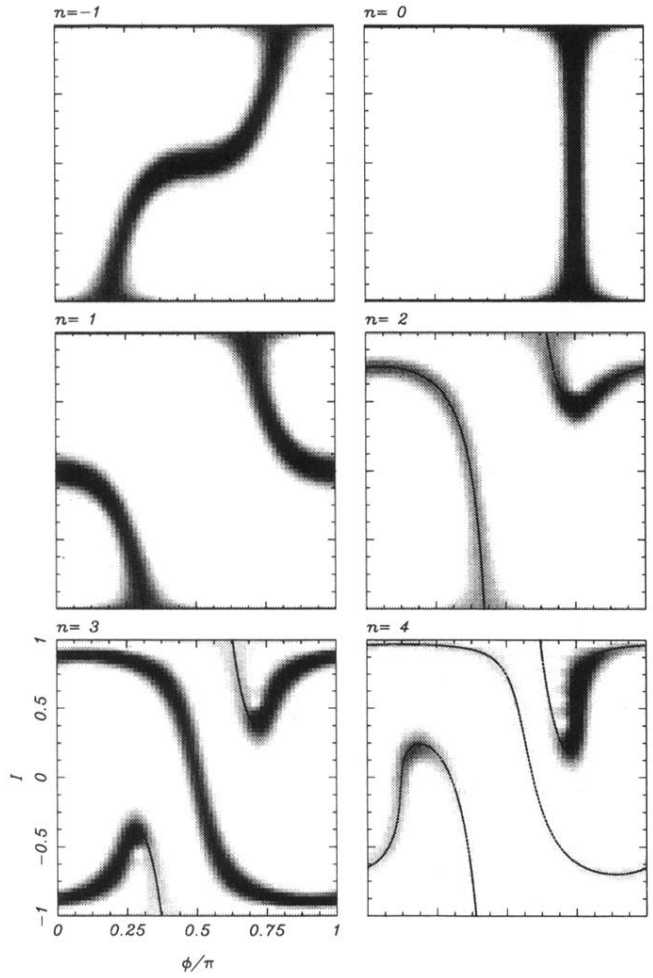

FIG. 7. Quantum symmetry lines $\mathcal{T}_n$ in Eq. (56) and corresponding classical symmetry lines $\Phi(T_{-1})$ [Eqs. (15), (29), (37), and (38)] for $k = 3$, $n = -1$ to 4, and $2J+1 = 128$.

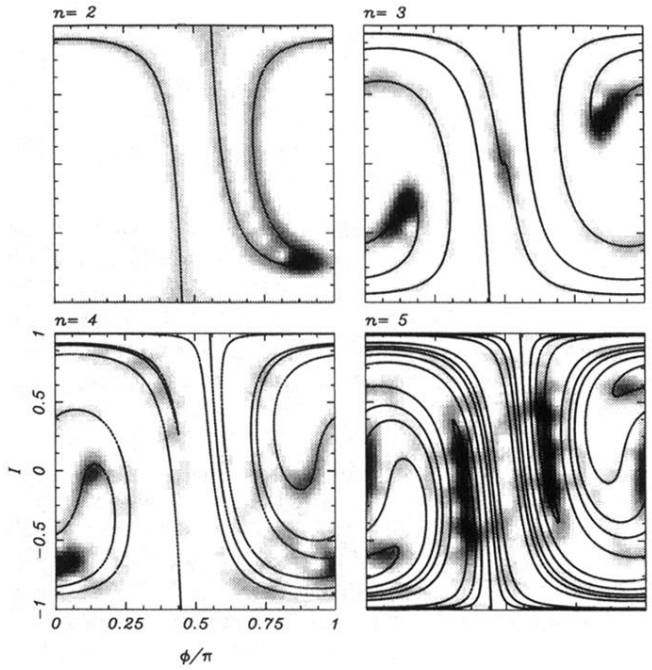

FIG. 8. The same as in Fig. 7 for $k = 6$, $n = 2$–5, and $2J + 1 = 128$.

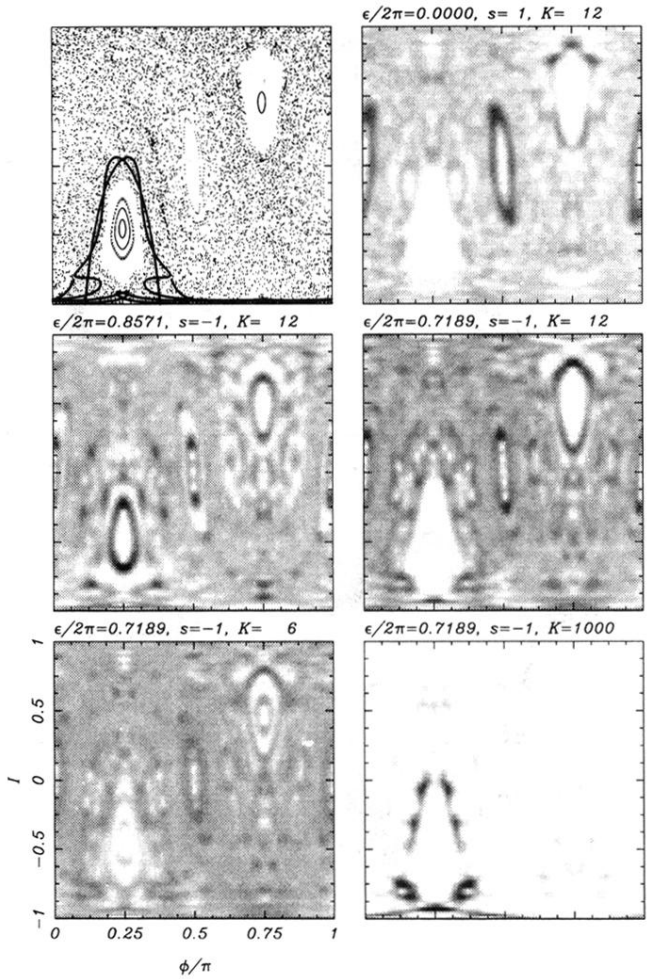

FIG. 9. Smoothed spectral intensity of Eq. (61) for $k = 3$, $2J + 1 = 1024$, and for some values of ϵ and smoothing time K. Only a parity $s = \pm 1$ corresponding to the eigenvalues of $\exp(-i\pi J)\hat{S}$ in Eq. (24) is selected (the phase factor in the parity definition has been added in order to avoid imaginary eigenvalues for half-odd J.) In the first frame a comparison to the classical phase-space diagram is given, and the stable and unstable manifolds of the $I = -1$ fixed point are drawn.